



Formation Mechanism of Pt Single-Crystal Nanoparticles in Proton Exchange Membrane Fuel Cells

P. J. Ferreira^a and Yang Shao-Horn^{b,*z}

^aMaterials Science and Engineering Program, University of Texas at Austin, Austin, Texas 78712, USA

^bElectrochemical Energy Laboratory, Massachusetts Institute of Technology, Cambridge, Massachusetts 02139, USA

In proton exchange membrane fuel cells, hydrogen permeated from the anode to the cathode was found to reduce soluble Pt species and produce faceted and dendritic Pt nanoparticles in the cathode ionomer. Moving away from the carbon support particles, the morphology of Pt nanoparticles changed from dendritic shapes to truncated tetrahedrons, truncated octahedrons, and truncated square cuboids. Transmission electron microscopy results suggest that the homogeneity of the driving force (supersaturation) for reduction of soluble Pt at the growing surface could dictate the transition from dendritic to faceted growth, and the competition between surface energy and interfacial kinetics of Pt reduction could govern the shape of faceted Pt nanoparticles. © 2007 The Electrochemical Society. [DOI: 10.1149/1.2431240] All rights reserved.

Manuscript submitted October 3, 2006; revised manuscript received November 9, 2006. Available electronically January 17, 2007.

The basic components of a proton exchange membrane (PEM) fuel cell consist of an anode for hydrogen oxidation, a cathode for oxygen reduction, and a proton-conducting membrane (typically Nafion, a sulphonated polytetrafluoroethylene) to conduct protons from the anode to the cathode. Both the anode and the cathode are made of a porous network of Pt nanoparticle catalysts supported on amorphous carbon and a proton-conducting ionomer, which provides active sites as well as electron and ion conduction in three dimensions. Supported Pt electrocatalysts are typically prepared by adsorption of colloidal Pt particles, which are produced from reactions of H_2PtCl_6 and sodium salts, on amorphous carbon support.¹ These supported Pt particles are typically quasi-spherical, on the order of 2–3 nm and exhibit a lack of facets.² Although Pt nanoparticles are very stable in acids at low electrode potentials such as 0.05 V vs the reversible hydrogen electrode potential (RHE), considerable dissolution of Pt has been reported at high potentials (0.90–1.1 V vs RHE),^{2–9} which reduces cathode activity and fuel cell efficiency. Recent studies^{2,6,10} have shown that dissolved Pt species in the cathode can react with H_2 molecules, which permeate through the proton conducting membrane from the anode, leading to the precipitation of Pt nanoparticles in the ion-conducting polymer. Pt nanoparticles formed at the membrane-cathode interface exhibit predominantly faceted shapes while those noted in the ionomer phase of the cathode are mostly dendritic.² The sizes and shapes of Pt nanoparticles formed in PEM fuel cells² resemble those of Pt colloidal nanoparticles prepared by chemical reduction of a Pt^{2+} or Pt^{4+} salt.^{11–16}

Despite these efforts, a detailed characterization of the various Pt nanoparticles formed across the cathode and at the membrane-cathode interface is still lacking. To address this gap, our work examines various Pt nanoparticles which precipitated off-carbon support in cross-sectioned cathode samples using high-resolution transmission electron microscopy (TEM). In particular, we were able to identify and correlate the shape and related crystallographic surfaces of precipitated Pt nanoparticles in PEM fuel cells to positions within the cathode and membrane-cathode interface. This work provides a deeper understanding of the formation mechanism of Pt nanoparticles in the PEM fuel cell cathode, which allows us to not only predict and reduce the surface area loss of Pt and activity loss of the cathode in PEM fuel cells, but also to provide new insights into the processes controlling the morphologies of Pt nanoparticles.

We propose that a nonuniform supersaturation of soluble Pt species at the growing nanoparticle's surface leads to the formation of dendritic Pt crystals in the cathode ionomer phase, while the degree of nonuniformity governs the transition from dendritic to faceted

growth of Pt nanoparticles. The competition between surface energy and interfacial kinetics for Pt reduction on distinct crystallographic surfaces, determines the shape of faceted Pt nanoparticles. In particular, the difference in the degree of hydrogen adsorption on Pt nuclei distributed in the cathode, the anisotropy of hydrogen adsorption on different Pt surfaces, and the anisotropy in interfacial kinetics for reduction of soluble Pt species and attachment of Pt atoms to a growing crystal surface, leads to the development of different Pt nanoparticles faceted shapes observed in the PEM fuel cell cathode.

Experimental

An ink made of 46 wt % Pt/Vulcan supported catalyst powder and Nafion ionomer solution was prepared, deposited to form the electrode layers and subsequently hot-pressed onto a 50 μm thick Nafion membrane. Both electrode layers had Pt loadings of 0.4 $\text{mg}_{\text{Pt}}/\text{cm}^2$ and they were assembled into 50 cm^2 cells, which were fed with fully humidified H_2 (counter electrode or anode) and N_2 (working electrode or cathode) at 80°C at ambient pressure. Although electrochemical reactions occurring in the working electrode were oxidative, the electrode was being used to model behavior in the cathode of working fuel cells. The cathode was cycled between 0.6 and 1.0 V (referenced to the anode, i.e., the RHE potential scale) at a sweep rate of 20 mV/s. Electrochemically active specific area (in $\text{m}^2/\text{g}_{\text{Pt}}$) of platinum in the cathode monitored by in situ cyclic voltammetry¹⁷ was found to decrease sharply upon cycling and 63% of the initial electrochemical surface area of Pt was lost after 10000 cycles.²

Cross-sectional TEM samples were prepared from the cathode cycled after 10000 cycles. A small strip was cut and mounted in epoxy, which was then cured at $\sim 60^\circ\text{C}$ for 12 h. Slices of the epoxy sample mount (100 nm thick) were produced by microtoming with a diamond knife such that a width-wise cross-sectional area was transparent to the electron beam. The cross-sectional thin slices were deposited subsequently on a carbon/copper grid for TEM observation in a JEOL 2010 FX operated at 200 kV.

Results and Discussion

TEM imaging of the cycled cathode cross sections revealed two distinct Pt nanoparticle types located off-carbon support in the ionomer—faceted type located adjacent to the membrane-cathode interface (Fig. 1) or in the cathode ionomer far from carbon-supported Pt particles (Fig. 2) and dendritic type (Fig. 3) located in the cathode ionomer adjacent to carbon-supported Pt particles.

Among the faceted type Pt nanoparticles, three distinct shapes were found—truncated octahedron (nanoparticle A in Fig. 1a), truncated square cuboid (nanoparticle B in Fig. 1a), and truncated tetrahedron (Fig. 2) shapes. To better illustrate the morphologies of these faceted Pt nanoparticles and the relations to the TEM images obtained, 3-D models and 2-D projections of these Pt nanoparticles are

* Electrochemical Society Active Member.

^z E-mail: ferreira@mail.utexas.edu; shaohorn@mit.edu

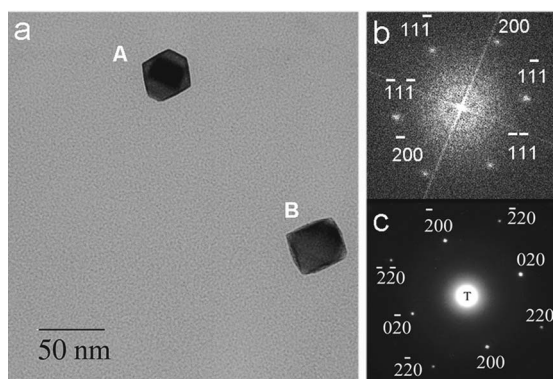


Figure 1. (a) Bright-field TEM image showing faceted Pt nanoparticles found at the cathode/membrane interface. (b) The $[01\bar{1}]_{Pt}$ fast Fourier transform pattern of nanoparticle A. (c) The $[00\bar{1}]_{Pt}$ electron diffraction pattern of nanoparticle B.

shown in Fig. 4. The TEM image of the Pt nanoparticle labeled A in Fig. 1a reveals the 2-D projection of a truncated octahedron parallel to an orientation close to the $[01\bar{1}]_{Pt}$ direction (Fig. 4a), which is further supported by the fast Fourier transform pattern of particle A in Fig. 1b. On the other hand, a careful analysis of the mass-contrast distribution around the edge of nanoparticle B in Fig. 1a and of the electron diffraction pattern taken from this nanoparticle (Fig. 1c) suggests a truncated square cuboid-type shape, where $\{100\}_{Pt}$ planes are predominantly exposed (Fig. 4b). Finally, high-resolution TEM images and electron diffraction data in Fig. 2 show that the Pt nanoparticle consists of large $\{111\}_{Pt}$ surfaces and narrow $\{100\}_{Pt}$ sur-

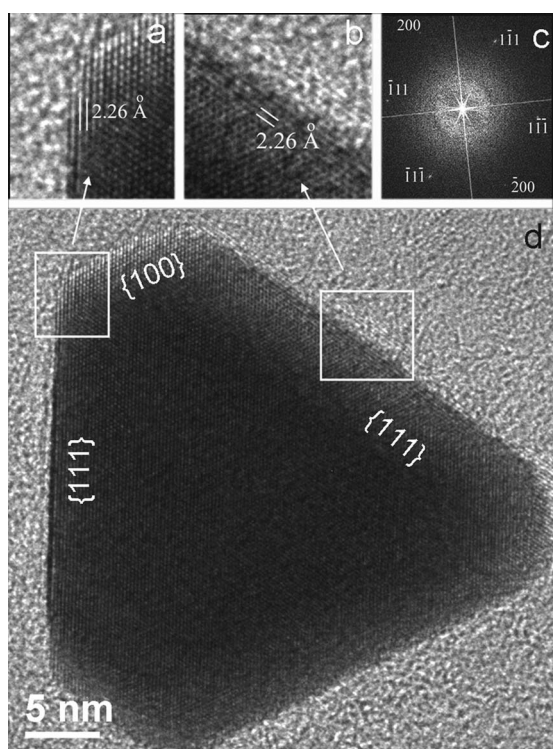


Figure 2. (a and b) High-resolution TEM images showing the interplanar spacing of $\{111\}_{Pt}$ planes on two crystallographic faces. (c) Fast Fourier transform pattern from the Pt particle shown in (d) taken with the beam parallel to the $[01\bar{1}]_{Pt}$ direction. (d) Pt nanoparticle with a truncated tetrahedron shape showing the various crystallographic faces.

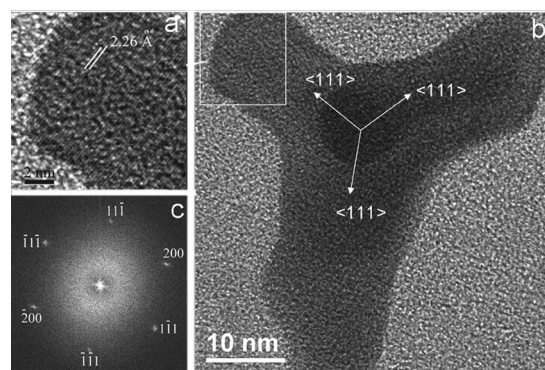


Figure 3. (a) High-resolution TEM image taken from the square region in (b) showing the interplanar spacing of $\{111\}_{Pt}$ planes. (b) Starlike shape Pt nanoparticle showing the growth of three arms along the $\langle 111 \rangle_{Pt}$ type directions. (c) Fast Fourier transform pattern taken from (b) showing the single-crystal nature of these star-like shape particles.

faces (Fig. 2a-d), from which a 3D model of a truncated tetrahedron can be constructed (Fig. 4c). The TEM image shown in Fig. 2d corresponds to a projection (Fig. 4c) taken with the beam direction parallel to the $\langle 110 \rangle_{Pt}$ type direction.

For the dendritic Pt nanocrystalline particles, found adjacent to carbon-supported Pt nanoparticles in the cathode ionomer (Fig. 3), high-resolution TEM images and electron diffraction analyses clearly show that these particles are single-crystals. A careful observation of Fig. 3 reveals that the dendritic arms grow along the

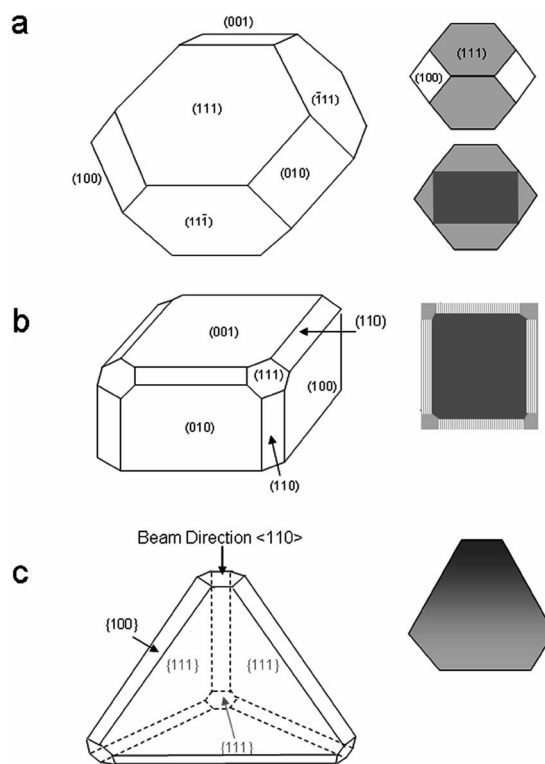


Figure 4. (a) Truncated octahedron shape of Pt nanoparticles using the Wulff construction. A 2-D projection parallel to the $\langle 110 \rangle_{Pt}$ direction is shown in the upper right. On the lower right, the mass-contrast exhibited by the nanoparticle is correlated with the variation in thickness. (b) Truncated cube-type shape of Pt nanoparticle. A 2-D projection parallel to the $\langle 001 \rangle_{Pt}$ direction is shown on the right. (c) Truncated tetrahedron shape of Pt nanoparticles. A 2-D projection parallel to the $\langle 110 \rangle_{Pt}$ direction is shown on the right.

$\{111\}_{\text{Pt}}$ directions, which is in good agreement with the lattice fringes shown in Fig. 3a and the Fourier transform pattern indexed along the $[011]_{\text{Pt}}$ zone axis in Fig. 3c. Similar morphologies (tetrapods) have been reported for CdSe nanoparticles.¹⁸

To understand the formation of these aforementioned distinct shapes, we first analyzed the concentration and distribution of H_2 molecules and soluble Pt species in the cathode, which will provide insights into the mechanisms of dendritic versus faceted Pt nanoparticles growth. In general, the availability of H_2 can play an important role in the surface energy of faceted Pt nanoparticles while the concentration and distribution of soluble Pt species in the cathode reflect the magnitude and homogeneity of the driving force for chemical reduction of the Pt species, which in turn will strongly affect whether the Pt nanoparticles will be of dendritic or faceted shape.

To evaluate the availability of H_2 molecules and soluble Pt species within the cathode, we start by estimating the flux of soluble Pt species generated during voltage sweep from 0.6 to 1.0 V vs RHE, according to the following expression

$$N_{\text{Pt}} = \frac{(c_{\text{Pt}}^{\text{V}_{\text{high}}} - c_{\text{Pt}}^{\text{V}_{\text{low}}}) \cdot L \cdot \nu}{V_{\text{high}} - V_{\text{low}}} \quad [1]$$

where N_{Pt} is the averaged flux of soluble platinum species generated during voltage sweep, L is the electrode thickness ($L = 10 \mu\text{m}$), ν is the sweep rate ($\nu = 20 \text{ mV/s}$), and $c_{\text{Pt}}^{\text{V}_{\text{high}}}$ and $c_{\text{Pt}}^{\text{V}_{\text{low}}}$ are the concentrations of soluble Pt species at the high ($V_{\text{high}} = 1.0 \text{ V}$) and low voltage ($V_{\text{low}} = 0.6 \text{ V}$) limits, respectively. It is assumed that $c_{\text{Pt}}^{\text{V}_{\text{high}}}$ approaches the equilibrium concentration at 1.0 V ($\sim 10^{-6} \text{ mol/L}$ according to Ferreira et al.²), and $c_{\text{Pt}}^{\text{V}_{\text{low}}}$ is equal to zero at 0.6 V. Based on Eq. 1, the estimated flux of soluble Pt species generated during voltage cycling of $5 \times 10^{-14} \text{ mol/s} \cdot \text{cm}^2$ is much lower than that of permeated hydrogen, which typically has values¹⁹ on the order of $\sim 8 \times 10^{-9} \text{ mol/s} \cdot \text{cm}^2$ ($\sim 1.5 \text{ mA/cm}^2$) for $50 \mu\text{m}$ Nafion membranes. As a result, the dissoluble Pt ionic species are nearly totally reduced at the membrane-cathode interface, where the permeated H_2 molecules enter the cathode. Moving away from the membrane-cathode interface, the concentration of soluble Pt ionic species in the ionomer should be higher, and become increasingly nonuniform, particularly close to the carbon-supported Pt nanoparticles. In addition, permeated H_2 molecules that are not consumed in the chemical reduction of soluble Pt species are likely to be electro-oxidized ($\text{H}_2 \rightarrow 2\text{H}^+ + 2\text{e}$) quickly on the carbon-supported Pt nanoparticles in the cathode at voltages in the range of 0.6 and 1.0 V vs RHE. As a consequence, the concentration of permeated H_2 molecules decreases from the membrane-cathode interface towards the cathode-diffusion media interface.

With the aforementioned considerations in mind, let us first consider the case of faceted Pt nanoparticles. It should be mentioned that these particles remain near the hydrogen potential even in the cathode because they are not in electrical contact with the cathode potential. In this case, the shape is controlled by minimization of surface energy and interfacial kinetics of Pt reduction and subsequent Pt atomic incorporation onto different Pt surfaces. From a thermodynamic point of view, the equilibrium shape of faceted Pt nanocrystalline particles will be determined by $\sum A_i \gamma_i = \text{minimum}$, where γ_i is the surface energy per unit area A_i of exposed Pt surfaces, if edge and curvature effects are negligible. For ideal face-centered-cubic (fcc) metals such as Pt, the surface energy of atomic planes with high symmetry should follow the order $\gamma\{111\}_{\text{Pt}} < \gamma\{100\}_{\text{Pt}} < \gamma\{110\}_{\text{Pt}}$ due to surface atomic density, which has been validated by recent theoretical studies of Skriver et al.²⁰ and Foiles et al.²¹ It has been reported²¹ that the surface energy of $\{100\}_{\text{Pt}}$ faces is 1.65 J/m^2 (153 kJ/mol per surface Pt atom), and it is 0.21 J/m^2 (37 kJ/mol) higher than that of the $\{111\}_{\text{Pt}}$ faces. On the basis of calculated surface energies, the equilibrium crystal shape can be created by the familiar Wulff geometrical construction.²² Frenken et al.²³ have reported that the equilibrium shape of a Pt

crystal at zero temperature should be a truncated octahedron consisting predominantly of $\{111\}_{\text{Pt}}$ and $\{100\}_{\text{Pt}}$ facets, as shown in Fig. 4a. Chemical adsorption of H_2 molecules should decrease the surface energy of Pt surfaces but the enthalpy and kinetics of H_2 adsorption depends on the crystallographic orientation. The enthalpy of H_2 adsorption on the $\{100\}_{\text{Pt}}$ surfaces is $40\text{--}50 \text{ kJ/mol}$ higher than the $\{111\}_{\text{Pt}}$ surfaces²⁴ and thus H_2 adsorption lowers the surface energy of $\{100\}_{\text{Pt}}$ surfaces in comparison to $\{111\}_{\text{Pt}}$ surfaces. In addition, open $\{100\}_{\text{Pt}}$ surfaces chemisorb H_2 gases more readily than the $\{111\}_{\text{Pt}}$ surfaces.²⁵ Therefore, the equilibrium shape of a faceted Pt nanocrystalline particle in the presence of H_2 will likely transform from a truncated octahedron shape (Fig. 4a) to a truncated square cuboid shape (Fig. 4b) as the fraction of the $\{111\}_{\text{Pt}}$ surfaces decreases to minimize the surface energy of Pt nanoparticles. This rationale is supported by many experimental observations reported previously. Wang et al.²⁶ have reported that heat-treating Pt nanoparticles in H_2 resulted in cubic Pt nanocrystals supported on SiO_2 and Al_2O_3 having predominantly $\{100\}_{\text{Pt}}$ surfaces, while heat-treating these cubic crystals in gases other than H_2 caused a transformation to spherical shapes. In addition, TEM measurements performed by Petroski et al.¹¹ have shown that a reduction of K_2PtCl_4 using H_2 , with or without low concentrations of capping polymer, lead to the formation of Pt cubic nanocrystalline particles. Increasing the amount of capping polymer on Pt nanocrystalline particles,^{12,13} which presumably prevents H_2 adsorption on Pt surfaces, appears to stabilize the $\{111\}_{\text{Pt}}$ surfaces relative to the $\{100\}_{\text{Pt}}$ surfaces, leading to the formation of Pt truncated octahedrons.

The three distinct shapes (truncated octahedron, truncated square cuboid, and truncated tetrahedron) found in this study differ in the fraction of $\{100\}_{\text{Pt}}$ surfaces relative to $\{111\}_{\text{Pt}}$ surfaces (Fig. 1, 2, and 4). It is believed that the formation of different faceted shapes resulted from the difference in the partial pressure of H_2 adjacent to Pt nuclei, in the membrane or in the ionomer phase of the cathode. The higher the partial pressure of H_2 , the greater fraction of $\{100\}_{\text{Pt}}$ surfaces relative to $\{111\}_{\text{Pt}}$ surfaces should be expected, for faceted Pt nanoparticles. This is consistent with the observation that truncated square cuboids were found close to the membrane-cathode interface. Moreover, as the structure of Nafion membrane and ionomer varies on the order of $10\text{--}20 \text{ nm}$,²⁷ the concentration of permeated H_2 might not be uniform in the ion-conducting polymer, which can lead to different levels of hydrogen adsorption on the $\{111\}_{\text{Pt}}$ and $\{100\}_{\text{Pt}}$ surfaces. Therefore, it is not surprising to observe both truncated octahedrons and truncated square cuboids near the membrane cathode interface (Fig. 1). On the other hand, as H_2 molecules can be electro-oxidized quickly on carbon-supported Pt nanoparticles in the cathode, the concentration of H_2 molecules in the cathode decreases considerably and the effect of hydrogen adsorption on the surface energy of Pt nanoparticles is reduced. Therefore, shapes other than truncated octahedrons and truncated square cuboids may form in the ionomer phase where the concentration of H_2 molecules is low (away from the membrane-cathode interface) and hydrogen adsorption on the Pt surfaces is not significant to produce $\{100\}_{\text{Pt}}$ faces with surface energy lower than that of the $\{111\}_{\text{Pt}}$ surfaces.

It has been shown that the transition from faceted to dendritic growth of Pt nanocrystals can be dictated by anisotropy²⁸ in the interfacial kinetics for reduction of soluble Pt species and subsequent incorporation of Pt atoms to a growing crystal surface, and by the magnitude²⁸ and/or uniformity²⁹ of the driving force (supersaturation) for hydrogen reduction of soluble Pt species at a growing surface, which largely depends on the concentrations of soluble Pt species and permeated H_2 to the growing crystal surface. Benjacob et al.²⁸ and Chernov²⁹ have discussed that faceted crystal growth develops at low driving forces (supersaturation) for a given value of anisotropy. Far from the carbon-supported Pt particles, the concentrations of hydrogen and soluble Pt species are uniform, and the driving force (supersaturation) of soluble Pt species is very small. Thus, faceted growth is expected and supported by our findings (Fig.

1 and 2). In this case, the formation of ridges is inhibited and the Pt nanoparticles will grow into a shape that is controlled by surface energy minimization and interfacial kinetics. As the surface energy of $\{100\}_{\text{Pt}}$ surfaces is lower than $\{111\}_{\text{Pt}}$ surfaces at high concentrations of H_2 , and interfacial kinetics of Pt attachment is more readily on $\{100\}_{\text{Pt}}$ surfaces than $\{111\}_{\text{Pt}}$ surfaces, square cuboid-like Pt nanoparticles with predominantly $\{100\}$ surfaces are expected, which is consistent with our findings (Fig. 1b). On the other hand, at low concentrations of H_2 or in absence of H_2 , truncated octahedron Pt nanoparticles (Fig. 1 and 4a) are expected from surface energy considerations. However, as $\{111\}_{\text{Pt}}$ surfaces are the least catalytically active for hydrogen reduction of soluble Pt species,³⁰ faster reduction and rapid attachment of Pt atoms on $\{100\}$ surfaces, rather than $\{111\}_{\text{Pt}}$ surfaces, lead to the formation of Pt nuclei having large $\{111\}_{\text{Pt}}$ surfaces, which could explain the formation of truncated tetrahedra far from supported Pt particles (Fig. 2). This hypothesis is consistent with the findings of Petroski et al.,¹¹ which show that Pt nanoparticles produced from hydrogen reduction of K_2PtCl_4 , upon initial growth or at high concentrations of capping polymer, were predominantly tetrahedron-like having $\{111\}_{\text{Pt}}$ surfaces.

Chernov²⁹ has shown that skeleton (extended at edges and corners) or dendritic growth can arise from an inhomogeneity in the driving force (supersaturation) on the growing surface. Near the carbon-supported Pt nanoparticles, the concentration of Pt species is relatively high and nonuniform along the growing surface, which is in good agreement with our finding that Pt nanoparticles adjacent to supported Pt particles are mostly dendritic. In addition, as the H_2 concentration in this region is low, it is believed that Pt nuclei exhibit primarily $\{111\}_{\text{Pt}}$ surfaces. Thus, any ridges formed on growing $\{111\}$ surfaces, which result in higher supersaturations, will tend to grow into dendritic arms. The outcome of this process is the formation of dendritic arms along the $\langle 111 \rangle_{\text{Pt}}$ directions, as shown in Fig. 3. Similar Pt dendritic crystals with $\langle 111 \rangle_{\text{Pt}}$ arms have been found by Xia et al.,¹⁴ after polyol synthesis of Pt nanoparticles, using H_2PtCl_6 , ethylene glycol and NaNO_3 at a relatively high supersaturation of H_2PtCl_6 .

Note that the experiments described above were carried out with nitrogen on the cathode (the working electrode) and hydrogen in the anode. As hydrogen was abundantly available in the cathode, Pt crystals produced from the chemical reduction of soluble Pt species were found near the cathode-membrane interface and in the cathode. However, in a working fuel cell, as the cathode environment is oxidizing due to the presence of oxygen, soluble Pt species can diffuse from the cathode into the membrane, become reduced by permeated H_2 molecules, and precipitate as Pt nanoparticles inside the membrane,² where the hydrogen concentration gradually increases from the membrane-cathode to the anode-membrane interface. Nevertheless, the formation mechanism of Pt nanoparticles in the ionomer and membrane proposed in this work should remain applicable.

Conclusion

In the cathode, dendritic Pt nanocrystals are predominant due to the fact that interfacial kinetics for reduction of soluble Pt species and incorporation of Pt atoms onto an atomically rough and growing surface is fast, relative to the diffusion of soluble Pt species to the surface of these dendritic Pt nanoparticles. On the other hand, near the cathode-membrane interface, faceted type Pt shapes are dominant because diffusion of Pt ions in the ionomer to the faceted Pt nanoparticles is fast, relative to interfacial kinetics of Pt addition on the growing faceted surfaces. Among the faceted type Pt shapes,

three distinct morphologies formed in the ion-conducting polymer of PEM fuel cells, namely truncated square cuboid, truncated octahedron, and truncated tetrahedron with increasing $\{111\}_{\text{Pt}}$ to $\{100\}_{\text{Pt}}$ surface ratios, which could result from the difference in the local partial pressure of H_2 adjacent to Pt nuclei. We propose that hydrogen adsorption lowers the surface energy of $\{100\}_{\text{Pt}}$ relative to the $\{111\}_{\text{Pt}}$ surfaces, which can be used to tailor and control the morphology of faceted Pt nanoparticles produced by hydrogen reduction of a Pt salt at low supersaturation.

Acknowledgments

This work made use of the TEM facilities at the Center for Nano and Molecular Science at the University of Texas at Austin, and the Shared Experimental Facilities at MIT supported by the MRSEC Program of the National Science Foundation under award no. DMR 02-13282. Y.S.H. acknowledges GM Fuel Cell Activities for financial support and the support of the DOE Hydrogen Initiative program under award no. DE-FG02-05ER15728. The authors thank H. Gasteiger, D. Morgan, and R. Makharia for stimulating discussions.

The Massachusetts Institute of Technology assisted in meeting the publication costs of this article.

References

1. S. Mukerjee and S. Srinivasan, in *Handbook of Fuel Cells: Fundamentals, Technology, Applications*, W. Vielstich, A. Lamm, and H. Gasteiger, Editors, p. 503, John Wiley & Sons, Chichester, U.K. (2003).
2. P. J. Ferreira, G. J. la O', Y. Shao-Horn, R. Makharia, and H. Gasteiger, *J. Electrochem. Soc.*, **152**, A2256 (2005).
3. P. Bindra, S. J. Clouser, and E. Yeager, *J. Electrochem. Soc.*, **126**, 1631 (1979).
4. M. Pourbaix, *Atlas of Electrochemical Equilibria in Aqueous Solutions*, Pergamon Press, Oxford (1966).
5. R. Woods, in *Encyclopedia of Electrochemistry of the Elements*, A. J. Bard, Editor, p. 1, Marcel Dekker, New York (1976).
6. T. Patterson, in *Fuel Cell Technology Topical Conference Proceedings*, G. J. Iqwe and D. Mah, Editors, p. 313, AIChE, New York (2002).
7. R. M. Darling and J. P. Meyers, *J. Electrochem. Soc.*, **152**, A242 (2005).
8. R. M. Darling and J. P. Meyers, *J. Electrochem. Soc.*, **150**, A1523 (2003).
9. X. Wang, R. Kumar, and D. J. Myers, *Electrochem. Solid-State Lett.*, **9**, A225 (2006).
10. J. Xie, D. L. Wood, K. L. Moore, P. Atanassov, and R. L. Borup, *J. Electrochem. Soc.*, **152**, A1011 (2005).
11. J. M. Petroski, Z. L. Wang, T. C. Green, and M. A. El-Sayed, *J. Phys. Chem. B*, **102**, 3316 (1998).
12. T. S. Ahmadi, Z. L. Wang, T. C. Green, A. Henglein, and M. A. El-Sayed, *Science*, **272**, 1924 (1996).
13. T. S. Ahmadi, Z. L. Wang, A. Henglein, and M. A. El-Sayed, *Chem. Mater.*, **8**, 1161 (1996).
14. T. Herricks, J. Y. Chen, and Y. N. Xia, *Nano Lett.*, **4**, 2367 (2004).
15. S. Y. Zhao, S. H. Chen, S. Y. Wang, D. G. Li, and H. Y. Ma, *Langmuir*, **18**, 3315 (2002).
16. J. Y. Chen, T. Herricks, and Y. N. Xia, *Angew. Chem., Int. Ed.*, **44**, 2589 (2005).
17. H. Gasteiger, W. Gu, R. Makharia, M. F. Mathias, and B. Sompalli, in *Handbook of Fuel Cells: Fundamentals, Technology, Applications*, W. Vielstich, A. Lamm, and H. Gasteiger, Editors, p. 593, John Wiley & Sons, Chichester, U.K. (2003).
18. L. Manna, E. C. Scher, and A. P. Alivisatos, *J. Am. Chem. Soc.*, **122**, 12700 (2000).
19. S. Kocha, in *Handbook of Fuel Cells: Fundamentals, Technology, Applications*, W. Vielstich, A. Lamm, and H. Gasteiger, Editors, p. 538, John Wiley & Sons, Chichester, U.K. (2003).
20. H. L. Skriver and N. M. Rosengaard, *Phys. Rev. B*, **46**, 7157 (1992).
21. S. M. Foiles, M. I. Baskes, and M. S. Daw, *Phys. Rev. B*, **33**, 7983 (1986).
22. G. Wulff, *Z. Kristallogr. Mineral.*, **34**, 449 (1901).
23. J. W. M. Frenken and P. Stoltze, *Phys. Rev. Lett.*, **82**, 3500 (1999).
24. N. M. Markovic and P. N. Ross, *Surf. Sci. Rep.*, **45**, 121 (2002).
25. R. J. Madix and J. Benziger, *Annu. Rev. Phys. Chem.*, **29**, 285 (1978).
26. T. Wang, C. Lee, and L. D. Schmidt, *Surf. Sci.*, **163**, 181 (1985).
27. A. L. Rollet, O. Diat, and G. Gebel, *J. Phys. Chem. B*, **106**, 3033 (2002).
28. E. Benjacob, R. Godbey, N. D. Goldenfeld, J. Koplik, H. Levine, T. Mueller, and L. M. Sander, *Phys. Rev. Lett.*, **55**, 1315 (1985).
29. A. A. Chernov, *Sov. Phys. Crystallogr.*, **16**, 734 (1972).
30. L. M. Falicov and G. A. Somorjai, *Proc. Natl. Acad. Sci. U.S.A.*, **82**, 2207 (1985).